Journal of Rock Mechanics and Geotechnical Engineering 18 (2026) 3640–3653

Contents lists available at ScienceDirect

Journal of Rock Mechanics and Geotechnical Engineering

journal homepage: www.jrmge.cn

Full Length Article

Propagation of rock fracture subjected to fluid injection using 4D X-ray computed tomography

Zizhuo Ma [a,c,e], Yibo Wang [a,c,*], Liang Zhao [b,c], Xinglin Lei [d], Yikang Zheng [a,c], Shaojiang Wu [a,c], Qingfeng Xue [a,c]

[a] Key Laboratory of Deep Petroleum Intelligent Exploration and Development, Institute of Geology and Geophysics, Chinese Academy of Sciences, Beijing, 100029, China
[b] State Key Laboratory of Lithospheric and Environmental Coevolution, Institute of Geology and Geophysics, Chinese Academy of Sciences, Beijing, 100029, China
[c] College of Earth and Planetary Sciences, University of Chinese Academy of Sciences, Beijing, 100049, China
[d] Geological Survey of Japan, National Institute of Advanced Industrial Science and Technology (AIST), Ibaraki, Japan
[e] Key Laboratory of Oil & Gas Reservoir Geophysics, SINOPEC, Beijing, 100083, China

ARTICLE INFO

Article history:
Received 2 January 2025
Received in revised form
23 July 2025
Accepted 22 August 2025
Available online 4 November 2025

Keywords:
Fluid injection
Sandstone failure process
In situ 4D X-ray computed tomography
Real-time direct identification of rock fracture propagation
Water-rock interaction analysis
Hydraulic connection channel

ABSTRACT

During unconventional energy extraction, substantial volumes of fluid are injected into low-permeability reservoirs to facilitate hydraulic fracturing, creating an extensive network of fractures that enhance fluid mobility. However, such large-scale fluid injection can lead to the initiation and propagation of fractures, potentially triggering detectable seismic events that pose risks to human life and infrastructure. To better understand these processes, in situ dynamic scanning imaging of hydraulic fracture propagation and water-rock interactions in tight sandstones has been conducted using X-ray computed tomography (CT). Our experimental findings reveal that fluid infiltration weakens rock strength, thereby promoting rock failure. Under the influence of fluid injection, microfractures undergo a continuous cycle of generation, expansion, and coalescence, ultimately forming interconnected hydrological pathways. These pathways are critical for the sustained propagation of fractures within the rock. CT imaging highlights a positive feedback loop between fracture growth and the enhancement of fluid diffusion. Notably, the rock at the dry-wet interface of the fluid front is particularly susceptible to fracturing. Additionally, the rates of fracturing vary among different fractures and tend to progressively decrease as the fractures extend deeper into the rock.

1. Introduction

In recent years, the role of exogenic fluids in anthropogenic seismicity (particularly fluid injection-induced earthquakes associated with energy exploitation) has garnered significant scientific and societal attention. Fluid injection-induced earthquakes remain a great threat to surrounding geological masses and residential structures (Shapiro and Dinske, 2009; Shelly et al., 2011; Yang et al., 2012; Ellsworth, 2013b; Schultz and Wang, 2020; Tan et al., 2020). As an effective means of energy exploitation, fluid injection has been widely used, including that in underground waste and saltwater disposal (Healy et al., 1968; Frohlich et al. 2011, 2014; Rubinstein et al., 2014; Foulger et al., 2018); enhanced geothermal system (EGS) development (Majer et al., 2007; Grigoli et al., 2018; Kim et al., 2018b; Lee et al., 2019; Schoenball et al., 2020; Yeo et al., 2020); hydrocarbon production(Wilson et al., 2017; Li et al., 2020); carbon dioxide capture, sequestration and underground gas storage (Cesca et al., 2014); hydraulic fracturing of rocks (House, 1987; Atkinson et al., 2020); and coal, mineral and ore mining (Foulger et al., 2018). However, several fluid injection-induced earthquakes with large magnitudes have occurred previously (Bao and Eaton, 2016). Since 2015, several hydraulic fracturing induced earthquakes (M_L 4.5+) have occurred in the Western Canada Sedimentary Basin (WCSB). The latest induced earthquake (M_L 5.2) occurred in November 2022 in

* Corresponding author. Key Laboratory of Deep Petroleum Intelligent Exploration and Development, Institute of Geology and Geophysics, Chinese Academy of Sciences, Beijing, 100029, China.
E-mail address: wangyibo@mail.iggcas.ac.cn (Y. Wang).

Peer review under responsibility of Institute of Rock and Soil Mechanics, Chinese Academy of Sciences.

https://doi.org/10.1016/j.jrmge.2025.08.024

the province of Alberta, and research has confirmed that it was directly related to nearby hydraulic fracturing operations (Peña Castro et al., 2020). Some earthquakes ($M_L \geq 4$) in the Central and Eastern United States are induced by wastewater disposal (Ellsworth, 2013b). Fluid injection for EGS development has also induced a M_W 5.4 earthquake in Pohang, South Korea (Kim et al., 2018a). In the Sichuan Basin of China, fluid injection operations such as wastewater disposal, salt mining, and hydraulic fracturing have induced earthquakes of different magnitudes (Lei et al., 2020). For example, hydraulic fracturing operations have caused several destructive earthquakes, including the M_W 4.7, M_L 5.7, M_L 4.9, and M_L 5.3 earthquakes in 2017, 2018, 2019, and 2019, respectively (Lei et al. 2017, 2019; Yang et al., 2020). In these industrial operations, large fluid volumes were injected into target geological formations. Thus, fluid-injection-induced earthquakes have caused a series of controversial problems (Lei et al., 2020). However, the rock failure process of fluid injection remains controversial (Berchenko and Detournay, 1997; Bohloli and De Pater, 2006; Arthur et al., 2009; Hu and Wang, 2018; Wang et al., 2021), and measures must be taken to conduct the operations safely and more efficiently. Thus, we are committed to investigating the role of fluids in the occurrence of fluid injection-induced earthquakes.

Understanding the rock failure process during fluid injection, particularly the hydraulic fracture propagation process, is crucial for ensuring the stability of the geological mass in the construction area and reducing the risk of induced earthquakes (Rutledge et al., 2004; Cui et al., 2013; Ellsworth, 2013a; Liu et al., 2014; Schultz et al., 2020; Schultz and Wang, 2020; Tan et al., 2020). Despite extensive research on the mechanisms of fluid injection-induced earthquakes, there remains a scarcity of direct observational evidence to substantiate existing research perspectives. Geological formations, being opaque media, pose challenges for the direct observation of rock failure processes within them. Furthermore, operational constraints of monitoring devices hinder real-time monitoring in high-temperature and high-pressure environments thousands of meters underground. Fortunately, laboratory simulations of field fluid injection construction provide convenient conditions for such research (Lei et al., 2016).

Investigating the role of fluids within rock failure mechanisms necessitates a comprehensive understanding of the mechanical deformation characteristics exhibited by fractured rock masses, as well as the growth dynamics of fracture networks. The nucleation and coalescence of fractures depend on the inherent properties of reservoir rock and its response to geological formation stress. The fracture propagation path is based on the reaction of fracture growth to injection operations, the mechanism of interaction with existing natural fractures, and the hierarchy of multiple fractures (Cao et al., 2021). Under these complex stress conditions, the mechanisms controlling fracture nucleation, generation, and growth are particularly important (Renard et al., 2019; Zang et al., 2021).

To elucidate the principles governing fracture growth within large-scale reservoirs, the deformation and fluid flow dynamics within geological formations must be observed. Microseismic monitoring and imaging techniques have been widely used for indirectly describing the spatial distributions of fractures and inferring fracture propagation patterns during field operations of hydraulic fracturing (Maxwell et al., 2010). However, the accuracy of fracture analysis may be significantly compromised by the suboptimal quality of microseismic signals acquired in field settings, along with the considerable expenses associated with field construction (Zang et al. 2017, 2021). Laboratory-based hydraulic fracturing experiments, characterised by their flexible design and robust operability, offer a viable alternative for simulating diverse operational conditions. In situ hydraulic fracturing experiments have progressively emerged as a conventional method for investigating the propagation characteristics of hydraulic fractures (Ma et al., 2022). Acoustic emission monitoring is an effective method to study the destruction process of the rock sample (Ishida et al., 2012; Rodriguez and Stanchits, 2017; Kwiatek et al., 2018; Gehne et al., 2019; Velcin et al., 2020), which can indicate the fracture pattern inside a rock sample (Naoi et al., 2025; Song et al., 2025). However, for small-scale rock samples, the location accuracy of acoustic emission events is limited.

Numerical simulation is also an effective method for studying the propagation process of hydraulic fractures. Xia et al. (2024) employed the rock failure process analysis (RFPA) method to establish a deep reservoir model that considers permeability anisotropy and conducted comparative research on the hydraulic fracture propagation law. Wei et al. (2024) established a hydraulic fracturing model based on the combined discrete element method (CDEM) and conducted numerical simulations on the propagation laws of hydraulic fractures. Based on the results of numerical simulation and spatiotemporal distribution characteristics of acoustic emissions during hydraulic fracturing, scholars have gained extensive insights into the propagation laws of hydraulic fractures (Liu et al., 2022). The propagation path of hydraulic fractures is controlled by the direction and magnitude of in situ stress, and bedding structures (such as bedding planes and natural fractures) also significantly influence the fracture propagation path (Zhang et al., 2023). However, during numerical simulation, the selection of input parameters and models, as well as the establishment of boundary conditions, can affect the simulation results, and the validity of numerical simulations relies on verification through experimental or field data.

The propagation of hydraulic fractures is the result of complex fluid-solid coupling interactions. However, methods based on acoustic emission monitoring or numerical simulations cannot effectively help investigate the underlying mechanisms of how fluids influence the effective stress field within rock matrices, dynamic initiation of hydraulic fractures, and their interactions with natural fractures (Li et al., 2023). X-ray computed tomography (CT) has been widely employed for directly revealing fluid flow through pores and the evolution of the internal structure in rock samples (Watanabe et al., 2011; Watanabe et al., 2013; Delle Piane et al., 2017; Jiang et al., 2017; Renard et al., 2017; Patmonoaji et al., 2019; Renard et al., 2019; Van Offenwert et al., 2019; Alhosani et al., 2020; Withers et al., 2021). In situ industrial X-ray microtomography (synchrotron radiation facility) has been successfully employed to monitor fracture growth within millimetre-scale samples under triaxial stress loading (Cartwright-Taylor et al., 2020). Nevertheless, when conducting in situ X-ray microtomography of rock fracture propagation under synchrotron radiation facility conditions, the utilised rock specimens are exceedingly diminutive (merely a few millimetres in size). Drilling water holes and conducting fluid injection in such small rock samples are difficult; thus, scholars can only observe the rock failure process under triaxial compression. Consequently, simulating the fluid injection process within geological formations under the aforementioned experimental conditions is unfeasible. Furthermore, the fractures observed in millimetre-scale rock specimens are of insufficient magnitude to be of practical significance for industrial applications. A more profound understanding of the rock fracture process can be attained through the investigation of fluid-rock interactions within geological formations. Medical X-ray tomography has proven to be an exemplary method for in situ research on the fluid transfusion process and growth of the hydraulic fracture network within centimetre-scale rock specimens (Ma et al., 2022).

In this study, based on in situ real-time X-ray imaging technology, the actual fracture propagation process within authentic centimetre-scale sandstone samples has been successfully documented and analysed under simulated formation pressure conditions. For the first time, the experimental results revealed a positive feedback mechanism between hydraulic fracture propagation and fluid seepage enhancement in tight sandstone. In this study, we demonstrated the preferential fracturing pattern at the dry-wet interface of the fluid front, elucidating the spatial selectivity of seepage weakening in rock failure mechanisms. Furthermore, the dynamic behaviour of microfractures is quantified in this study by proposing a three-stage 'generation-propagation-connection' evolutionary model, indicating that the formation of seepage channels primarily depends on nonlinear fracture coalescence processes. Additionally, we elucidated the attenuation law of fracture propagation rates: competitive propagation exists among different fractures, with fracturing rates exhibiting exponential decay as fractures extend deeper into the rock. According to the above fluid-structure interaction phenomenon observed during the experiment, new evidence is provided for the mechanism of fluid injection-induced earthquakes.

2. Experimental details

2.1. Experimental facility

To accurately obtain the variation law of the internal structure of rock samples during fluid injection, we independently built a set of experimental equipment apparatus. The independently developed experimental apparatus is capable of simulating a pseudo-triaxial stress field and the fluid injection process, while simultaneously enabling in situ real-time CT scanning of rock samples. A detailed description of the method and apparatus is presented by Ma et al. (2022).

The independently developed experimental setup comprises two parts: (1) the aluminium alloy core holder that can withstand ultrahigh pressure, and (2) a pressure loading system to simulate pressure conditions. Another part of the experimental system is the third-generation medical X-ray CT scanner, which is used to image the sample placed in the core holder. The schematic diagram of the experimental system is shown in Fig. A1. The pressure loading system is used to simulate the actual formation stress state, and the hydraulic fracturing process includes three syringe pumps (Fig. A1) to control the confining, axial, and water injection pressures. All three pressure pumps are electrically controlled to ensure stable operation during the hydraulic fracturing experiment, and the control software can remotely control the continuous pressure setting and recording (Ma et al., 2022).

As the key goal of this experiment is to determine the evolution of the internal rock structure during the fluid injection experiment, the X-ray CT scanning image quality should be as high as possible. The core holder we used independently met two important criteria simultaneously. One is the excellent mechanical performance capable of withstanding ultrahigh pressure to ensure the safety of the experiment. The other is appropriate X-ray penetrability to ensure the quality of the X-ray CT scanning image. According to previous studies, we found that the aluminium alloy material is suitable (Shi et al., 2011; Akbarabadi and Piri, 2013; Wenning et al., 2019). Aluminium alloy has very good mechanical properties but a very low density of approximately ~2.75 g/cm^3, and its X-ray attenuation coefficient is relatively low. To determine the most suitable core holder thickness for the experiment, we conducted a series of tests. The core holder was designed to withstand confining and axial pressures up to 50 MPa and 100 MPa, respectively. We adopted the method of controlling variables for testing. First, we prepared cylindrical sleeves comprising aluminium alloy with thicknesses of 8 mm, 9 mm, 10 mm, 11 mm, and 12 mm, and placed them with the rock sample for CT scanning. By comparing the resolution of the CT images, we found that the 11- and 12-mm thick sleeves can cause artifacts in CT imaging. Therefore, we excluded these two thicknesses. Subsequently, we conducted a one-week pressure limit test using the remaining sleeves, with test pressures higher than the set confining and axial pressure values. After the test, we measured whether the deformation of the sleeves was within the normal range. The 8- and 9-mm thick sleeves exceeded the prescribed deformation range after the pressure test; thus, only the 10-mm thick sleeve met the requirements. Therefore, the thickness of the aluminium alloy core holder was finally set to 10 mm.

To ensure the integrity of the sample within the core holder during the experiment and prevent fluid leakage between the rubber sleeve and the sample, two measures were implemented. First, experiments were conducted using tight sandstone samples with extremely low permeability. Prior to the experiment, the samples were meticulously polished with sandpaper to achieve a smooth surface, ensuring a snug fit between the rubber sleeve and the sample. Under the high confining pressure conditions of the experiment, there was virtually no gap between the rubber sleeve and the sample, thereby preventing fluid circulation. Second, the plugs at both ends of the sample were designed with grooves and sealing rings to further mitigate the risk of fluid leakage.

The utilisation of synchrotron radiation facilities for the imaging of in situ dynamic fracture propagation within rock samples under triaxial stress loading serves as a robust foundation for this study. Nevertheless, the X-ray tomography scan duration of synchrotron radiation facilities, which can extend up to several minutes, may not effectively capture rapid hydraulic fracture expansion (Renard et al., 2017). Furthermore, the sample must be rotated to complete CT scanning with the synchrotron radiation facility. In our study, to preserve the absolute static state of the rock samples and promptly ensure the completion of CT scanning, the medical scanner emerged as a viable option. We selected the latest generation of medical scanners, called GE Revolution CT, produced by the General Electric Company. The scanning parameters of this medical CT scanner are excellent. The detector has a width of 160 mm and can rotate 360° around the rock sample. All the CT scans in one complete experiment use the same set of scanning parameters. The voltage and current are set to 140 kV, 300 mA, respectively; the time to complete one CT scan is set to 0.5 s (two frames per second); the pixel spatial resolution is set to 0.23 mm; and the pixel matrix size is 512 × 512 pixels (Ma et al., 2022). The spatial resolution of the medical equipment is sufficient to observe fractures inside centimetre-scale samples. To capture rapid fracture propagation, the extremely high temporal resolution of the medical X-ray scanner can compensate for some disadvantages in spatial resolution compared with the higher spatial resolution of industrial X-ray scanners. Besides, the CT scanning data for mapping in subsequent sections have already been denoised, including removal of ring artifacts and beam hardening.

2.2. Geological features of the experimental samples

We conducted a laboratory fluid injection experiment using tight sandstone samples collected from a tight sandstone gas reservoir. The total reserves of tight sandstone gas have reached 1/3 of China's total natural gas reserves. Therefore, the exploitation of tight sandstone gas has become the most important and realistic area of unconventional natural gas extraction in China in the future. The Sichuan Basin in western China is the main natural gas-producing area in the country. The exploration of moderate-depth

and shallow continental tight sandstone in the Sichuan Basin has a long history. Several tight oil and gas reservoirs have been found in the Jurassic Shaximiao Formation (Wang et al., 2020).

The samples used in this study were obtained from the Jurassic Shaximiao Formation in the central Sichuan Basin. Before starting the fluid injection experiment, we measured the physical parameters of 30 test samples. The mineral composition of the tight sandstones was determined through X-ray diffraction (XRD) analysis; the tight sandstones comprised quartz, feldspar, and clastic mica. The average quartz, feldspar, muscovite, and clay mineral contents were 69.1 %, 7.8 %, 2.6 %, and 20.5 %, respectively. The permeability and porosity of the sample were obtained by standard gas measurement. Based on the measurements, the average porosity and permeability were 8.5 % and 0.03 mD, respectively. The average grain size of the rock was 0.25 mm. The compressive and tensile strengths of the dry sample were 45.4 MPa and 15.18 MPa, respectively. Before the experiment, the tight sandstone sample was processed into a straight cylinder. The length and diameter were 125 mm and 50 mm, respectively. A water injection hole with a diameter of 6 mm and a length of 80 mm was drilled from the top of the sample (Fig. 1).

2.3. In situ fluid injection CT scanning experiment

The purpose of this experiment is to investigate the fracture propagation during fluid injection. According to the depth range of the target reservoir from 1500 m to 2500 m, we select the lithostatic pressure range from 15 MPa to 25 MPa. Considering the direction and value of the maximum horizontal principal stress in the reservoir, the axial pressure was set to vary between 80 MPa and 100 MPa. The setting range for the fluid injection pressure was from 10 MPa to 35 MPa. Based on the method of controlling variables, we conducted tests with a step size of 5 MPa within the aforementioned ranges of axial, confining, and injection pressures. A total of 27 experiments were conducted within the core holder pressure limitation. Each sample in the experiment was successfully fractured. Although the internal fracture network morphology of different samples after fracturing is not completely consistent, they all exhibit strong commonality. The experimental results presented in this study are the most typical results after comparison. After comparative analysis of the test experiments, the optimal pressure combination setting was finally determined (Fig. 2).

The experiment illustrated in Fig. 3 was conducted at room temperature and under nominally dry conditions. The duration of the entire experiment was approximately 180 min. The pressure

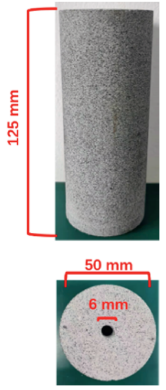

Fig. 1. Schematic images of the sample. After sample preparation, the sandstone sample used in the study was a cylinder measuring 125 mm and 50 mm in length and diameter, respectively. A water injection hole was drilled on one side of each sample, measuring 6 mm in diameter and 80 mm in length, respectively.

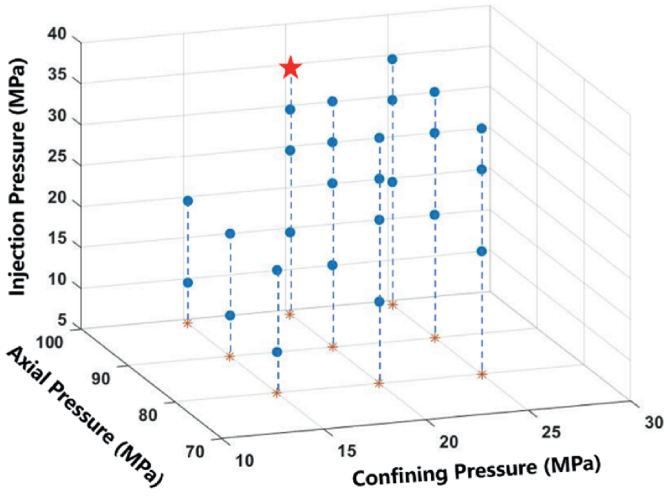

Fig. 2. Schematic diagram of the pressure combination settings. Blue dots represent different pressure combination settings. Orange asterisks represent pressure values projected onto confining and axial pressure planes. The red pentagon marks the optimal pressure combination setting.

loading during the experiment was set according to the optimal pressure combination obtained from previous test experiments: the maximum confining, axial, and injection pressures were 20 MPa, 99 MPa, and 37 MPa, respectively. The experimental conditions were relevant for the brittle deformation of rocks at depths of approximately 2 km (Renard et al., 2019). According to the pressure loading, the entire experiment included five stages: (I) coaxial loading, (II) increasing differential stress, (III) water injection, (IV) continuous fracture and (V) fracture completion stages (Fig. 3). During the entire hydraulic fracturing experiment, numerous of CT scans were conducted to observe the structural evolution inside the tight sandstone sample. The CT scan times are marked by the vertical lines in Fig. 3.

The first CT scan was conducted on the tight sandstone sample at zero stress as a reference to obtain the initial state of the sample before loading. Subsequently, the first stage of the experiment began, during which two CT scan images (Nos. 2 and 3) were obtained to determine the sample state after coaxial pressure. Thereafter, the experiment entered the second stage, during which the differential stress experienced six increments from 0 to 79 MPa. A total of six CT scan images (Nos. 4–9) were obtained after each stress increment during this stage. Subsequently, fluid was injected into the dry sandstone sample in creep form at the beginning. Previous numerical studies, along with the results of microseismic monitoring, have indicated that in hydraulic fracturing experiments, when the injection rate is set to a continuously increasing mode, the hydraulic fracturing effect is the best (Wang et al., 2016). In this stage, the fluid was injected with a gradually increasing injection rate setting for the syringe pump. The specific injection scenario followed three steps. Step 1: The injection pressure was increased from 0 to 10 MPa at a rate of 1 mL/min. Step 2: The injection pressure was increased from 10 MPa to 20 MPa at a rate of 1.5 mL/min. Step 3: The injection pressure was increased from 20 MPa to 30 MPa at a rate of 2 mL/min. A total of six CT scans (Nos. 10–15) were obtained after each pressure increment. The fourth stage was the continuous fracture process of the sandstone sample. At the beginning of this stage, the syringe pump was set at a rate of 5 mL/min to increase the injection pressure from 30 MPa to 35 MPa. When the injection pressure reached the target pressure, the sandstone sample rapidly began to fracture. The entire fracture stage lasted for approximately

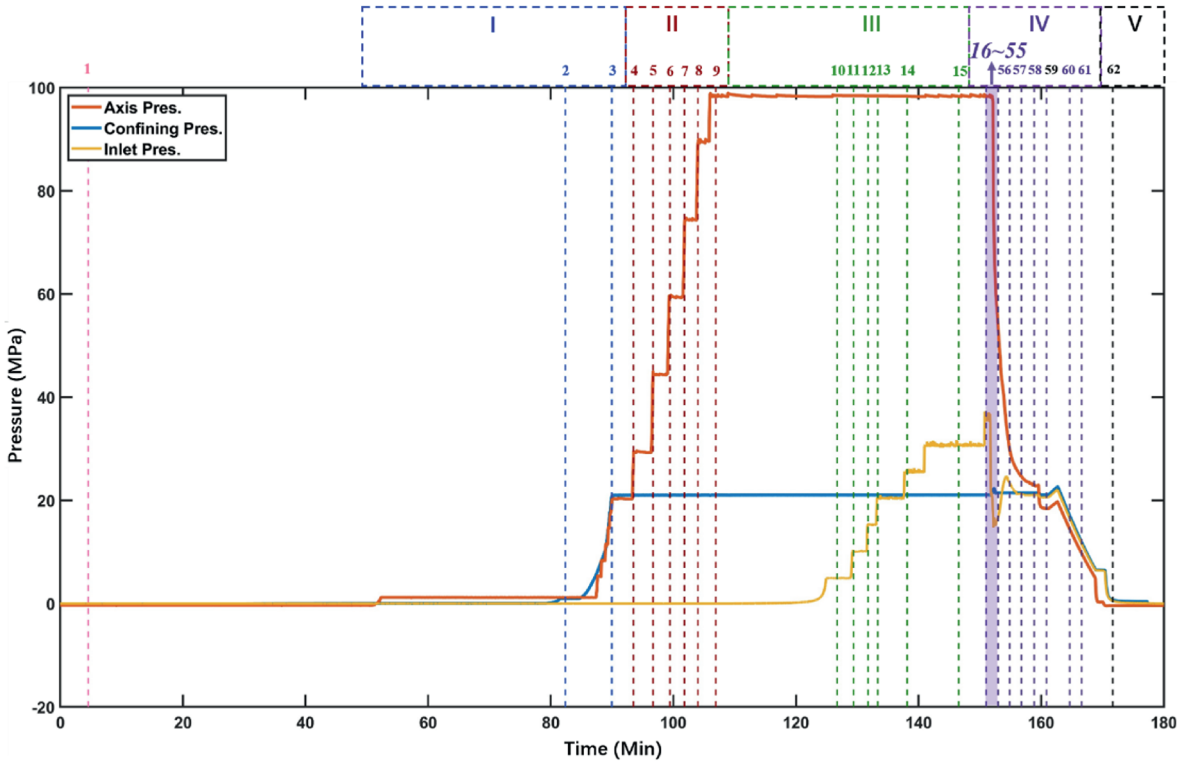

Fig. 3. Pressure loading curve for the fluid injection experiment. The blue, orange, and yellow lines represent the loading curves of confining pressure, axial compression, and injection pressure, respectively. The hydraulic fracturing experiment comprises five stages, where the blue, red, green, purple, and black dotted boxes indicate the coaxial loading (I), increasing differential stress (II), water injection (III), continuous fracture (IV), and fracture completion (V) stages, respectively. The CT scanning times during the entire hydraulic fracturing experiment are indicated by dotted lines of different colours and corresponding numbers. The pink vertical dotted line identifies the first CT scan of the sample in a stress-free state; the blue vertical dotted line indicates the two CT scan times for the coaxial loading stage; the red vertical dotted lines indicate the six CT scan times for the increasing differential stress stage; the green vertical dotted lines indicate the six CT scan times for the third stage; the purple rectangular block and another six purple vertical dotted lines indicate the CT scan time for the continuous fracture stage; and the black vertical dotted line indicates the CT scan time for the fifth stage.

20 min and can be divided into two parts. Part 1 represented the initial rapid fracture process with an extremely short time. During this part, forty three-dimensional (3D) X-ray tomography scans (Nos. 16–55) were obtained to indicate the drastic change in internal structure in the sandstone sample. The results of the 40 CT scan images were obtained in continuous scanning mode. The time to complete one CT scan was 0.5 s; the CT scan time interval between two adjacent scans was 2.5 s; and the total time was 120 s. The times of the 40 scans are marked by a purple rectangular block in Fig. 1. Part 2 represented the fracture development process. During this part, the axial stress, confining pressure, and injection pressure were finally decreased synchronously. In this part, six 3D X-ray tomography scans (Nos. 56–61) were used to indicate the continuous evolution of fractures in the sandstone sample. The fifth stage was the fracture completion stage. In this stage, all types of pressure were unloaded, which marked the end of the hydraulic fracturing experiment, and the CT scan No. 62 was conducted.

3. Results

We conducted a total of 62 CT scans to track the evolution of the internal structure during the experiment (Fig. 3). In this study, we focus on the results of the first 55 CT scan images.

3.1. Evolution of the fracture network in two-dimensional (2D) slices

In this section, 16 representative 3D X-ray tomograms in sequence are selected for analysis (Figs. 4 and 5). Video 1 in Appendix B shows a total of 40 CT scan images of the rapid process of internal structure evolution.

The initial CT scan image depicted the pristine structural integrity of the sample, characterised by randomly dispersed mineral particles and the absence of pre-existing fractures (Fig. 4a). A total of fifteen 3D X-ray tomograms (1st to 15th CT scan images) were acquired to monitor the structural evolution before fracturing (Video 1 in Appendix B). We selected seven 3D X-ray tomograms to introduce the specific phenomena.

Under the sustained application of coaxial pressure, the green dot area (high-density area) progressively expanded in the CT scan images (Fig. 4b and c). We inferred that with increasing coaxial pressure, some pre-existing micropores closed, implying compaction. When the differential stress reached the maximum value in the increasing differential stress stage (II), the high-density area in the sample increased further, indicating a deeper degree of compaction (Fig. 4d).

As shown in the images, the injection of fluid changed the completely dry state inside the sandstone sample. Concurrently, the injection pressure increased with injection time, and the continuous green area around the injection hole gradually expanded in the CT scan images (Fig. 4e–h). This phenomenon indicates that with increasing injection time and pressure, water gradually migrated from the injection hole into the rock matrix. Owing to the compactness of the sample, even during the latter period of this stage, only the rock matrix around the injection hole reached the fluid saturation state.

During the experiment, to investigate the changes in the internal structure of the sample with greater precision, we incorporated

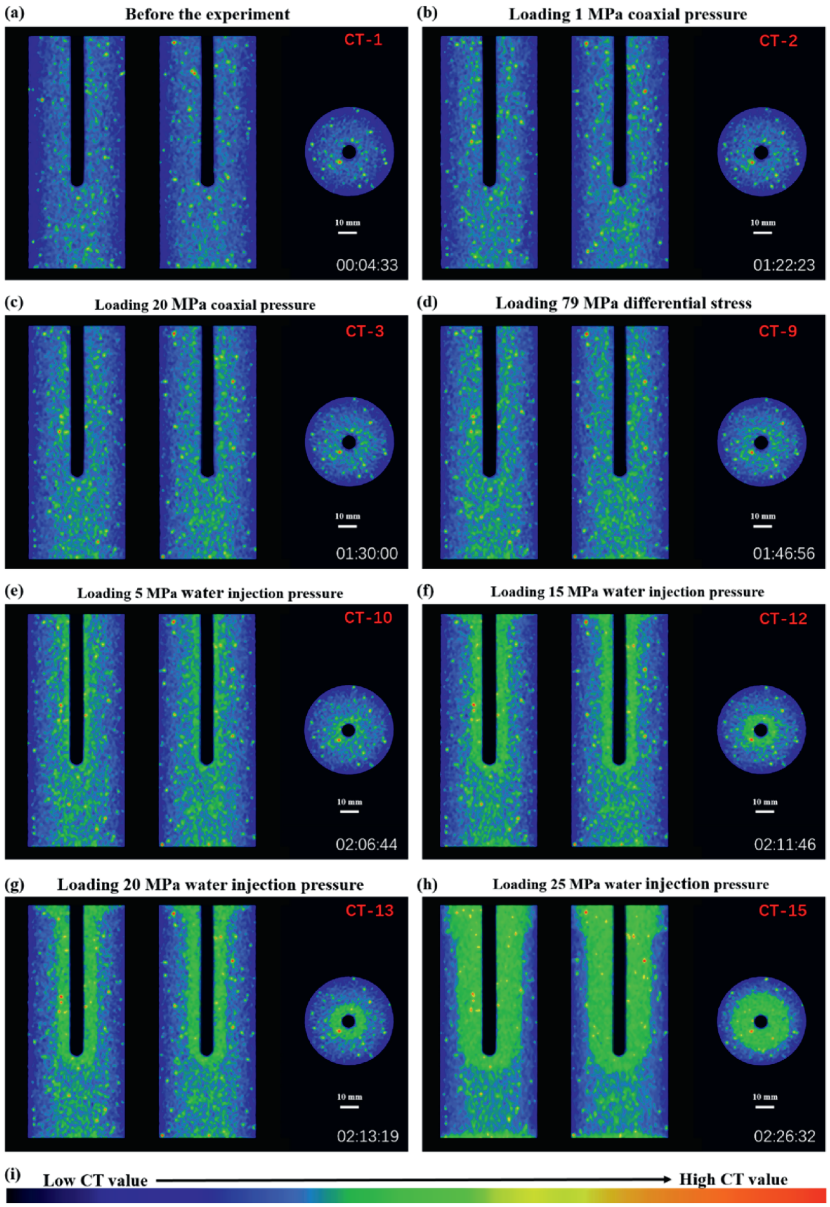

Fig. 4. Comparison of computed tomography (CT) slices of the internal structure of the sandstone sample before fracturing in the experiment. The CT scan images of each group are acquired at approximately the same position in the sample. Specific position descriptions and image feature descriptions of each group image are shown in Fig. A2. The red letters in each figure mark the number of the CT scan, and the white letters mark the time of the current CT scan (relative time from the start of the experiment). The colour bar of the image: the colours from black to red represent the changes in CT values from low to high.

slices extracted from different axial positions for comparative analysis (as shown in Fig. A3). At the inception of the fracture process (Fig. 5a), a narrow fracture was observed, forming an angle of 30° with respect to the σ_1 direction. This is in accordance with the value range in the Mohr-Coulomb criterion, which posits that the angle between the rock fracture surface and maximum principal compressive stress is $\left(45^\circ - \frac{\varphi}{2}\right)$, where φ represents the internal friction angle of rock, and the value of φ is usually 30°.

After propagating for 18 s (Fig. 5b), the narrow fracture extended into a region characterised by diverse mineral compositions, resulting in a noticeable deflection of its propagation direction, marked by the red box labelled No. 1. Additionally, the symmetrical position relative to fracture No. 1 was marked by the orange box labelled No. 2. A microfracture, marked by a white circle No. 3, occurred beneath the bottom of the injection hole (refer to the position marked by the dashed line No. IV in Fig. A3), and the direction of this microfracture was consistent with the dry-wet interface in this area. After extending for 18 s (Fig. 5c), the microfracture marked by white circle No. 3 gradually developed into a macrofracture along the dry-wet interface. At the position corresponding to dashed line No. V in Fig. A3, we observed another microfracture generated at the dry-wet interface marked by purple circle No. 4. After extending for 12 s (Fig. 5d), a pair of new fractures formed, marked by the pink box No. 5. This pair of new fractures and the existing fractures were axisymmetric about the axial direction of the sample. The microfracture marked by the purple circle No. 4 also gradually developed along the dry-wet interface. After extending for 24 s (Fig. 5e), microfracture No. 4 finally developed into a macrofracture. The No. 5 fractures enlarged and generated cross-fracture branches. At the position corresponding to

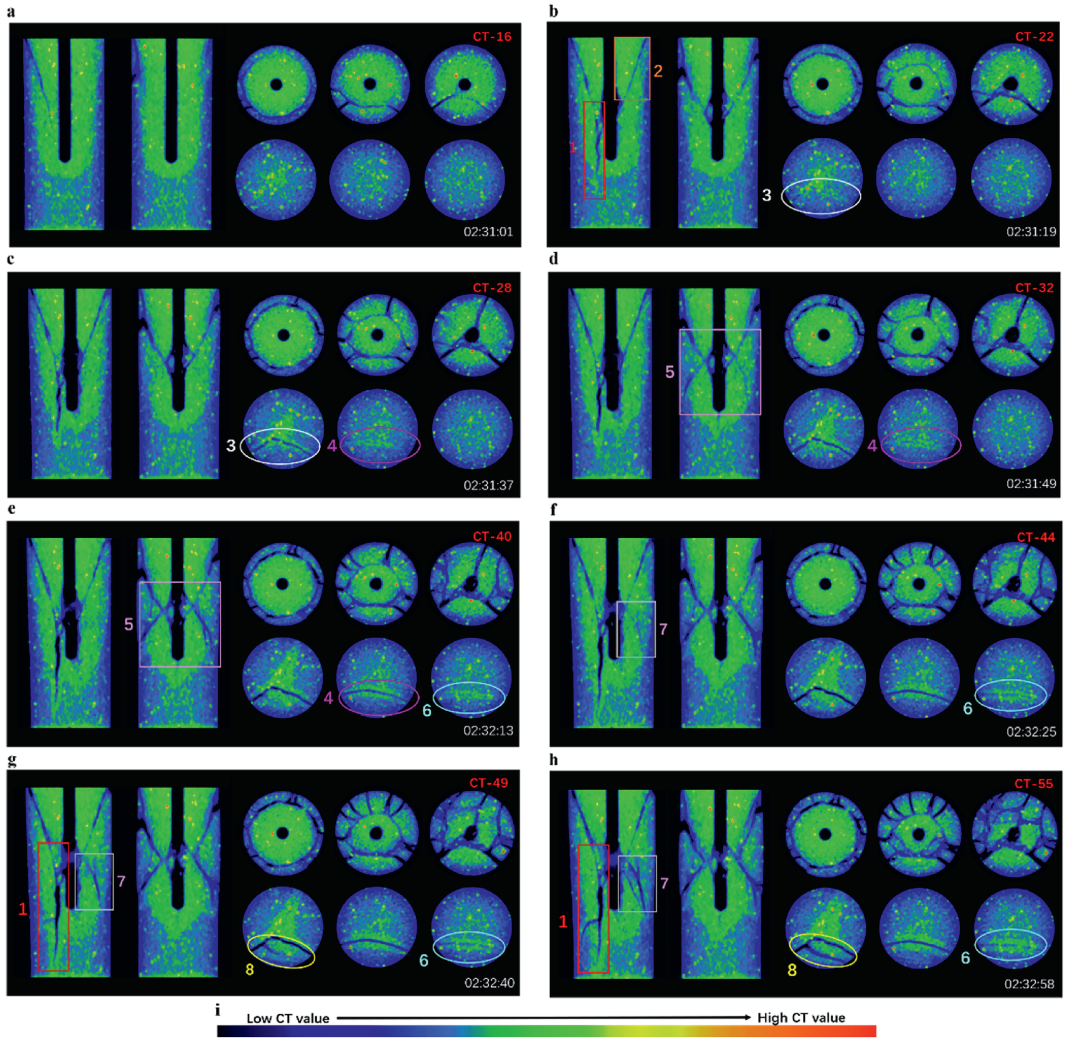

Fig. 5. Comparison of CT slices of the internal structure of the sandstone sample during the fracture process in the experiment. A total of six axial slices represent the six important positions of the sample, marked in Fig. A3.

the No. VI dashed line in Fig. A3, we observed another microfracture generated at the dry-wet interface marked by a blue circle No. 6. After extending for 12 s (Fig. 5f), a cross-microfracture formed at the end of the No. 2 fracture, marked by the grey box No. 7. After extending for 15 s (Fig. 5g), a secondary fracture nearly perpendicular to the direction of the maximum principal compressive stress was produced based on the large fracture extending to the bottom of the sample, marked by red box No. 1. The volume of the Nos. 6 and 7 fractures were significantly enlarged. Additionally, another secondary fracture was generated based on No. 3 fracture, and its expansion direction was also along the new dry-wet interface of the area. This fracture was marked by a yellow circle No. 8. After extending for 18 s (Fig. 5h), the secondary fracture in the red box No. 1 began to deflect, and its propagation direction changed from initially perpendicular to the maximum principal compressive stress to parallel to it. The original No. 7 cross-fracture enlarged, and a new fracture was generated nearly parallel to it. The No. 8 secondary fracture continued to expand.

3.2. Evolution of the fracture network in 3D volume

In the previous section, we analysed the fracture propagation pattern according to the CT slice images. To more comprehensively investigate the fracture propagation process, we focused on the propagation of the three-dimensional fracture network inside the rock sample. A detailed analysis of the fracture propagation process during the fluid injection experiment was performed using VG Studio Max software (V3.3) (Volume Graphics GmbH, Germany) to extract the fracture network and calculate the fracture volume from 40 CT scan datasets. The use of CT data to directly extract the fracture structure can help determine the growth of the real fracture network in the rock sample.

The gradually increasing slope of the curve of water injection rate reflects the transformation process of the internal structure of the rock (purple solid line in Fig. 6). During the initial stage, the injection volume showed a slow increase. After 20 min, the slope of the injection curve exhibited a marked enhancement, with this inflection point corresponding to structural alterations in the internal permeability of the rock. After 25 min, fracture initiation occurred within the sample, accompanied by a substantial increase in fluid migration channels, which increased the injection volume to sustain fracturing pressure. This phenomenon serves as a critical engineering indicator for evaluating the maturity of fracture network development.

The 40 values of fracture volume calculated by the software are projected onto the pressure curve to analyse the evolution of

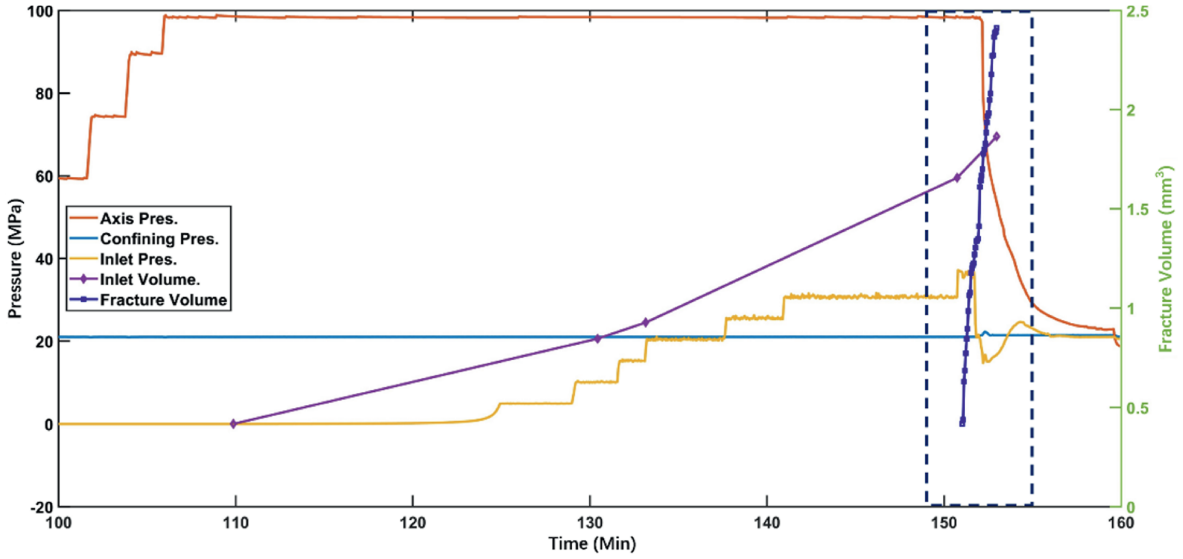

Fig. 6. Curve of the change in fracture volume with pressure loading during the hydraulic fracturing experiment. This curve mainly represents the stage when the pressure curve changed dramatically in the latter stage of the hydraulic fracturing experiment.

internal fracture volume with changing pressure over time after the start of fracturing, as shown by the blue dashed-dotted line in Fig. 6. According to the slope change of the curve of change in water injection volume, the water injection volume increased steadily. During the fracture process, the water injection volume increased rapidly.

Fig. 7 shows five representative CT scanning results selected from the 40 fracture networks from four perspectives extracted by the software. Video 2 in Appendix B shows a total of 40 groups of fracture network structures from four perspectives extracted by the software. As shown in Fig. 7, the connected fractures are marked with the same colour, and the same colour scheme is used to mark the fractures from small (blue) to large volumes (red). To describe the fracture propagation process, the fractures are marked in numbered boxes according to the positions of spatial distribution in the image, consistent with the marking order in CT images in the previous section.

In the first stage, the whole fracture morphology and volume changed dramatically. The comparison between the 16th (Fig. 7a) and 19th CT scan results (Fig. 7b) indicates that the fracture marked in the first red box experienced fracture deflection. The deflection direction is approximately 17°, and this deflection angle falls within the range of 10°–20° of local crustal stress field deflection in the Sichuan Basin (Ning et al., 2024). This indicates that fracture propagation is controlled by the redirection of regional tectonic stress. The second orange box shows the generation of the new fracture, which propagated at an angle of 30° with respect to the direction of the maximum principal compressive stress. It reveals the regulatory effect of sandstone weakness planes on fracture trajectories, which is consistent with the modified Coulomb fracture criterion.

In the second stage (Fig. 7c), the whole fracture morphology and volume did not change dramatically. We chose the representative 31st CT scan result, indicating that the fracture network was clearly expanded relative to the original network. The two fractures marked in the red box No. 1 and the orange box No. 2 merged with each other. Hydrological pathways include microfractures and pores in rock that facilitate fluid migration. Compared with that in pores, fluid migration is more likely to occur in fractures. The coalescence of two fractures signifies the formation of

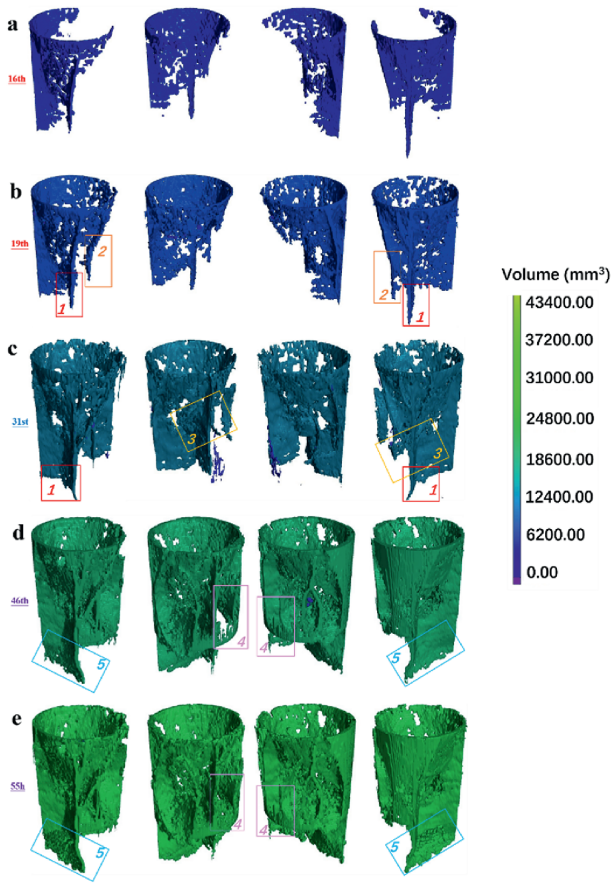

Fig. 7. Schematic images of the fracture propagation process inside the sandstone sample. The sequential order of the results is the 16th, 19th, 31st, 46th, and 55th CT scans. The legend on the right represents the corresponding colour scale value of the fracture volume.

dominant hydrological pathways. The deflection degree of the No. 1 fracture increased. A new fracture branch formed and propagated at an angle of 30° with respect to the direction of the

maximum principal compressive stress, marked by the 3rd box (yellow).

In the third stage, the whole fracture morphology and volume also changed dramatically. The 46th CT scan result (Fig. 7d) shows that a complex annular fracture surface was generated, marked by the No. 4 pink box. Additionally, at the bottom of the fracture network, a secondary fracture branch expanded perpendicular to the direction of the generated maximum principal stress, marked by blue box No. 5. This indicated that the boundary effect had a significant influence on fracture evolution. In the 55th CT scan results (Fig. 7e), the direction of expansion of the secondary fracture branch marked by blue box No. 5 changed, and it was no longer completely perpendicular to the direction of the maximum principal stress but tended to grow towards the bottom of the rock sample.

Integrated analysis of fracture network evolution across three stages reveals partial fracture closure in localised regions during the fracturing process. This phenomenon indicates a competitive mechanism between the directional propagation of secondary fractures and stress shadowing effects from dominant fractures. Such competition induces intermittent opening-closing behaviour in effective conductive channels, providing a crucial theoretical foundation for optimising the pumping protocols in fracturing design.

3.3. Calculation of the fracture propagation rate

According to a series of CT images obtained during the experiment, we found that the fracture rate was not uniform throughout the entire process. There were obvious differences in fracture propagation velocity at different positions in the early stage of the experiment. We selected three groups of representative images to illustrate the specific fracture evolution pattern and slip velocity. For comparison, we focused on several typical fractures in the sample. The changes in the propagation velocity or slip velocity of these typical fractures during the entire experiment were calculated.

For each selected fracture, we delimited a unified area to conduct measurements and calculations. When calculating the fracture propagation rate or fault slip rate, the areas delineated in the same group of images were used. The increase in propagation length was measured along the direction of fracture propagation. The increase in propagation width was measured by considering five equidistant points on the target fracture and subsequently calculating the average value. The propagation rate was calculated based on the expansion time.

Three examples are described below. In the first example, we selected the results of the 19th and 20th CT scans. In this example, we focused on the propagation rate of three fractures, as shown in Fig. 8. After calculation, the propagation rates of these three fractures were different. The growth rate of the newly deflected fracture (No. 1) was approximately 5.3×10^{-3} m/s. The growth rate of another new fracture (No. 2) was approximately 3.5×10^{-3} m/s. The propagation rate of the No. 3 fracture was considerably slow, at approximately 1.7×10^{-4} m/s. In the second example, we selected the results of the 22nd and 24th CT scans. The propagation rate of the No. 1 fracture was approximately 7.9×10^{-4} m/s. The propagation rate of the No. 2 fracture was approximately 8.8×10^{-5} *m/s*. The propagation rate of the No. 3 fracture was approximately 4.2×10^{-5} m/s. In the third example, we selected the results of the 27th and 30th CT scans. The propagation rate of the No. 1 fracture was approximately 8.8×10^{-5} m/s. The propagation rate of the No. 2 fracture was approximately 5.8×10^{-5} m/s. The propagation rate of the No. 3 fracture was approximately 2.9×10^{-5} m/s.

To summarise, with the continuous injection of fluid, the fractures had a wide range of propagation rates, which can be attributed to the heterogeneity in the internal structure and complexity of the mineral composition. We can summarise that the rate of fracture growth/propagation gradually decreased with time. According to the laboratory measurements, the order of magnitude of the growth rate of new fractures in the rock sample was 10^{-3} m/s, and that of the fracture propagation rate crossed an order of magnitude from 10^{-4} m/s to 10^{-5} m/s.

4. Discussion

4.1. Fracture network propagation process of the sandstone sample during fluid injection

In this study, for the first time, we innovatively employ in situ observation technology to comprehensively reveal the rapid hydraulic fracturing process (<30 min) of sandstone from the intact matrix, microfracture generation and macroscopic fracture network. Compared with conventional acoustic emission monitoring (Lei et al., 2000) or post-fracture CT scanning, we achieve the four-dimensional visualisation of the complete fracture process (nucleation-propagation-interaction) through synchronised pressure-CT-fluid tracing technology (Video 1 in Appendix B). Thus, we provide direct experimental evidence for unravelling the dynamic competition mechanisms governing hydraulic fracture propagation.

Lei et al. (2000) proposed an additional strain field at the process zone, which includes the tensile (volume strain increase) and compressive modes (volume strain decrease). The front of the propagating shear fracture is prone to expand towards the tensile direction, which contributes to the deflection(Lei et al., 2000). In our experiment, the process zone of the No. 1 fracture, marked in Fig. 5 and Video 1 in Appendix B, follows this propagation mechanism. The fracture initially propagated along a direction with an angle of 30° with respect to the direction of the maximum principal compressive stress σ_1. Under the effect of the local stress field at the process zone, the propagation direction gradually deflected towards the σ_1 direction. Finally, the No. 1 fracture propagates along the σ_1 direction. Moreover, many studies have indicated that some special phenomena may occur during the shear fracture propagation. For example, inclined and normal shear fracture zones may be created between the pre-existing and wing fracture zones (Lajtai, 1974; Vásárhelyi, 2006). In our experiment, the process zone of the No. 5 and No. 7 fractures, marked in Fig. 5 and Video 1 in Appendix B, follows this propagation mechanism.

For the first time, this experiment captured the dynamic details of the 'water precursor effect'. According to the typical propagation of the No. 1 fracture, we concluded that water plays the most important role in fracture propagation. According to the dynamic in situ CT scanning images obtained during the hydraulic fracturing experiment, we can determine the position of the fluid front based on the spatial distribution of CT values of the sample. In the process of continuous propagation, we found that the water front was always ahead of the fracture front, implying that water can drive the expansion of the fracture. With the continuous injection of high-pressure water, water-rock interaction occurred inside the sandstone, and the strength of the sandstone was weakened owing to the action of water. The effect of water pressure promoted the connection of pores between mineral particles in the sandstone, resulting in the loose arrangement structure of mineral particles. Some microfractures of extremely small scales began to appear inside the sandstone. Microfractures acted as important hydraulic connection channels, such that a steady stream of water converged at the microfractures. Under the continuous collection of water,

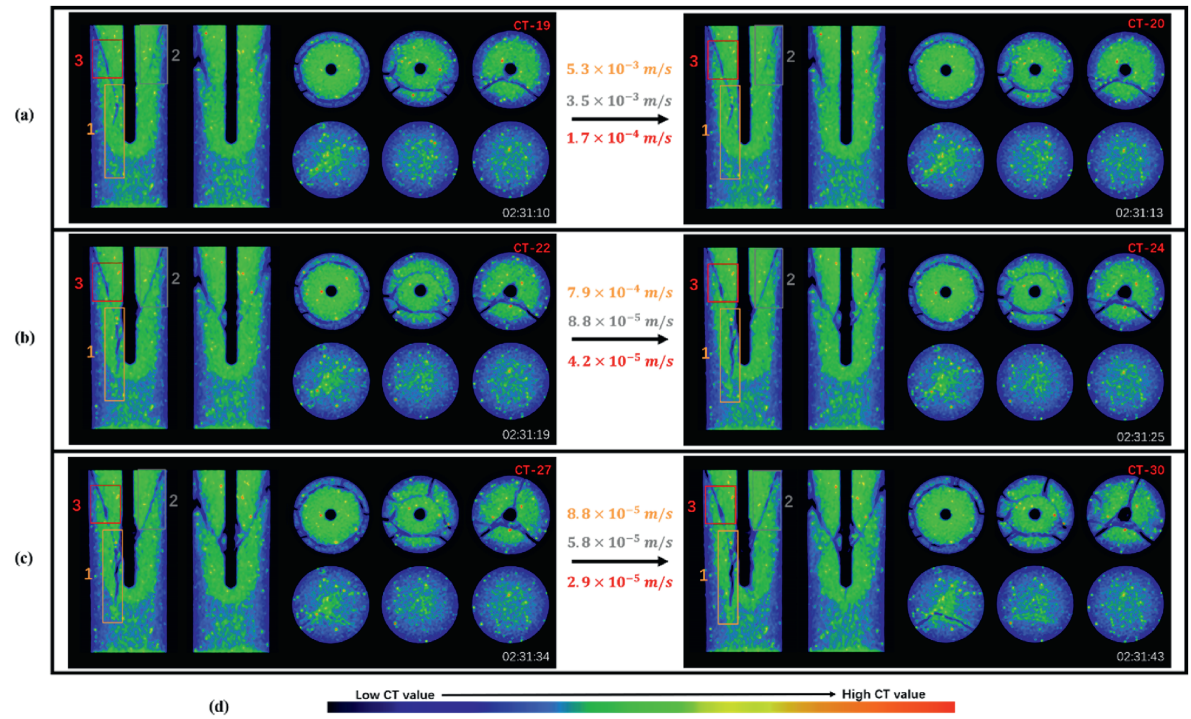

Fig. 8. Velocity calculation results of different parts inside the sample during the hydraulic fracturing experiment. (a) Velocity calculation results based on the 19th and 20th CT scan images of the sandstone sample. (b) Velocity calculation results based on the 22nd and 24th CT scan images of the sandstone sample. (c) Velocity calculation results based on the 27th and 30th CT scan images of the sandstone sample.

the pore pressure in this area continued to increase, and the effective positive stress continued to decrease, resulting in the propagation of microfractures.

The dry-wet interface was easily damaged at first, and the fracture easily propagated from the dry area far from the injection position to the wet area close to the injection position. We analysed that the effective normal stress is low owing to the high pore pressure in the wet area. The pore pressure is low and the effective normal stress is high in the dry area. The fracture was easily propagated from the area with high effective normal stress to that with low effective normal stress. Moreover, fractures easily propagated along the edge of the dry-wet interface. Owing to the complex stress state of the interface area, the angle deflection easily occurs when the fracture expands. This phenomenon confirmed the guiding effect of the unsaturated seepage field on the fracture process.

Macro fractures were developed based on microfractures. In the initial stage of fracturing, the distribution of microfractures was discrete. With the continuous injection of high-pressure fluid, the microfractures continued to expand and connected to form macro-fractures. Previous numerical simulations (Li et al., 2020; Rabbel et al., 2020) based on the extended finite element method (XFEM) or other numerical models have been conducted to study the fracture network evolution during hydraulic fracturing. These studies suggest several kinds of fracture development during rapid internal fluid generation in the rock sample, including individual fracture propagation, interaction and coalescence (Li et al., 2020; Rabbel et al., 2020). The conclusions of numerical simulations serve as a powerful theoretical basis for explaining the experimental phenomena observed in this study.

The specific evolution of fractures during the fracture process was also highly complicated. In the early stage of the fracture process, the expansion process of the fracture network was accompanied by the emergence of new fractures and closure of old fractures, which is consistent with the conclusions of previous studies (Renard et al., 2019; Rabbel et al., 2020). Many studies have shown that the interaction between fractures may alter the way that hydraulic fractures propagate, resulting in a compound fracture network. There are several reported types of fracture interactions, including crossing, slippage, dilation, activation, and deflection (Bongole et al., 2019). Phenomena corresponding to these types of fracture interaction were observed in our experiment. Main fracture propagation activated the surrounding microfractures and formed secondary fractures, and cross fractures were easily produced. Moreover, the early fracture network, which was initially formed in the sample, deeply affected the subsequent fracture development and propagation process. Fracture arrest, diversion, or offset were observed when a fracture encountered the existing fracture network. These conclusions can also be confirmed by previous numerical simulations (Rabbel et al., 2020).

4.2. Typical rock failure phenomena in the process of fluid injection

In this experiment, we observed some special rock failure phenomena during fluid injection. Here, we summarise four typical rock failure phenomena induced by fluid injection, according to the typical schematics of fracture propagation.

The first phenomenon is the generation of the isolated fracture. During the fluid injection experiment, an isolated fracture was generated far from the existing main fracture network, indicated by an orange dashed box in the fracture extraction results of the 19th, 20th and 21st CT scans (Fig. 9a). Notably, the continuous injection of fluid can increase the volume and mass of the permeable main fracture network, resulting in changes in the regional gravity load and pore thermoelastic effect. The poroelastic coupling-induced earthquake model posits that fluid injection/extraction can alter the pore pressure in rock layers, which

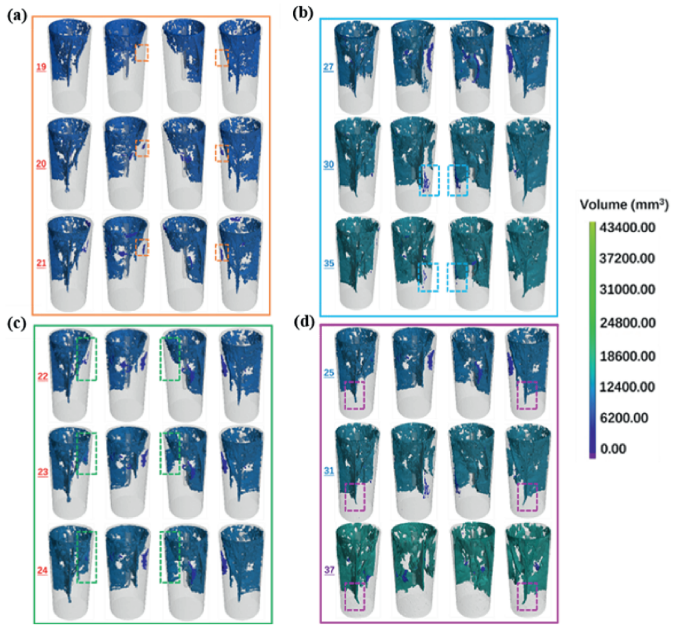

Fig. 9. Four rock failure phenomena during the process of fluid injection. The legend on the right marks the corresponding colour scale value of the fracture volume.

in turn adjusts the in situ stress field through pore-elastic effects (coupled fluid-solid mechanics). An increase in pore pressure reduces the effective normal stress. When the shear stress τ exceeds the critical frictional strength, the pre-existing fault becomes unstable and slips (Ellsworth, 2013b). These changes can cause the rupture of the intact area far from the main fracture network. However, we propose different views in this study. Despite the absence of a clear, direct hydraulic channel facilitating fluid diffusion between the isolated fracture and the existing main fracture network, the continuous injection of fluid can stimulate the ongoing creation of microfractures at certain distances from the injection hole. These microfractures serve as pathways, enabling the fluid to gradually spread to regions far from the hydraulic channel and ultimately induce the formation of new fractures.

The second phenomenon is the hydraulic fracture propagation. During the fluid injection experiment, new fracture branches were generated on the edge of the existing main fracture network and continued to expand, indicated by the green dotted line in the fracture extraction results of the 22nd, 23rd and 24th CT scans (Fig. 9b). The connected main fracture network can provide a good hydraulic channel. Fluid diffusion can continuously increase pore pressure in the edge area of the fracture network, which can activate the weak surface in the critical state in the area. The weak surface can easily slide. Macroscopically, the existing large fracture network can continue to expand. This view is consistent with the pore pressure diffusion model (direct induced earthquake model) promoted by Ellsworth (Ellsworth, 2013b).

The third phenomenon is the split and closure of the fracture. During the fluid injection experiment, the fracture branch at the edge of the main fracture network slipped under the combined action of pore pressure and regional stress and separated from the main fracture network, indicated by the blue dotted box in the fracture extraction results of the 27th and 30th CT scans (Fig. 9c). Subsequently, the volume of this isolated fracture gradually decreased, indicated by the blue dashed box in the fracture extraction results of the 30th and 35th CT scans (Fig. 9c). The isolated fracture experienced the process of continuous closure and compaction. The fracture closure is driven by dual mechanisms: (1) the stress shadow effect leads to the redistribution of confining pressure, increasing the normal stress on the fracture surface; (2) coupling of fluid seepage-stress induces pore structure collapse, with CT value analysis revealing a decrease in matrix porosity around the fractures. This process fundamentally represents the relaxation of the fracture system from a non-equilibrium state to a thermodynamically stable state. This phenomenon unveils the self-organised criticality of hydraulic fracture systems. When injection pressure exceeds the rock damage threshold, the fracture network dissipates energy through branch splitting. During the injection-pause periods, the system restores local stress equilibrium through the closure of secondary fractures. This dynamic equilibrium mechanism provides laboratory evidence for explaining the 'pressure oscillation-fracture reconstruction' cycle observed in field fracturing operations. Notably, in engineering practice, a pulsed injection strategy should be adopted to regulate such processes, which can enhance the stability of flow conductivity.

The fourth phenomenon is the deflection of the fracture. During the fluid injection experiment, the fracture propagation front clearly deflected with the continuous propagation of the fracture, marked by the pink dashed box in the fracture extraction results of the 25th, 31st and 37th CT scans (Fig. 9d). Owing to the complex distribution of mineral components inside the rock sample, the overall internal structure was nonuniform. In areas where certain distributed minerals have higher density and intensity, the rock matrix areas have lower density and relative intensity. During the expansion of the fracture front, if it encountered a mineral aggregation area with high strength, it was prone to deflection, and subsequently, it tended to bypass this area and expand along the low intensity area, which is more conducive to expansion. Moreover, the existence of the dry-wet interface can also be an important factor leading to fracture deflection.

4.3. Knowledge of the fracture generation and propagation mechanism during fluid injection

Previous studies have indicated that fracture propagation inside the rock during high-pressure fluid injection corresponds to seismic activity. The fracture is formed in areas where seismic events accumulate, and the fracture will subsequently propagate rapidly. The fracture distribution inside the rock coincides with the seismic source distribution (Benson et al., 2020; Du et al., 2020). Therefore, the analysis of the mechanism of fracture generation and propagation during fluid injection is an important reference for understanding the seismogenic process of induced earthquakes.

Considering the mechanism of fluid injection-induced earthquake, Ellsworth (Ellsworth, 2013a) proposed two widely recognised end-member models: (1) the direct induced model implies that an induced earthquake is caused by the direct effect of fluid injection and (2) indirect induced model implies that an induced earthquake is caused by the change in solid-state stress, owing to fluid injection and extraction (Ellsworth, 2013a; Atkinson et al., 2016; Bao and Eaton, 2016; Kim et al., 2018b; Li et al., 2019; Zhang et al., 2019; Schultz et al., 2020; Tan et al., 2020). Eyre (Eyre et al., 2019)) proposed a third induced model combining the above two models, wherein dynamic rupture at the end of an existing fault can be caused by aseismic sliding driven by pore pressure. Fluid injection can easily cause aseismic slip along a fault near the injection well. Its accumulated strain can be transmitted along the fault, further loading the brittle fracture area with high strength far from the well.

However, our experimental results are not completely compatible with previous descriptions of the rock failure

mechanisms induced by fluid injection. Our experimental results can provide information regarding the mechanism of fracture generation and propagation. In general, fluids play vital roles in failure areas. In the process of fault instability and slippage, owing to the strong thermal pressurisation effect caused by the fluid, the stratigraphic rock can easily reach an unstable critical state. Once the pore fluid pressure exceeds the minimum compressive stress, the rock will rupture. Moreover, owing to the heterogeneity of geological formations, the rupture process in the source zone is complex. The rupture rate in the source zone is localised. The rupture rate range measured in the laboratory is $10^{-3} - 10^{-5}$ m/s. The rate of rupture at different spatial locations at the same time is different. The rupture rate at the same spatial position is also different at different times, and the rupture rate at the beginning of rupture is higher than that in the subsequent rupture stages.

Based on the aforementioned analysis, the fracture mechanism revealed by the experiment can be further summarised into two distinct evolutionary phases. (1) Fluid-driven activation of pre-existing weak planes: the pore pressure gradient may trigger the tensile propagation of natural microfractures, forming permeability-enhanced zones. (2) Self-organised critical propagation: the primary fracture may regulate the growth and propagation of the secondary fracture network through the stress shadowing effect. The controlling role of geological heterogeneity in fracture mechanisms manifests in three key aspects. (1) Mineral-cemented weak planes as preferential conduits: CT images show that macroscopic fractures tend to develop along feldspar-quartz grain boundaries. (2) Stress rotation-induced fracture deflection: the presence of mineral grains and local microfractures can cause the deviation of the local principal stress direction, leading to the deviation of fracture paths from the σ_1 direction and forming complex network structures. (3) Multiscale fracture velocity coupling: there is a two-order-of-magnitude difference between the microfracture propagation rate (10^{-5} m/s) and macroscopic fracture rate (10^{-3} m/s), which also conforms to the law of energy dissipation and explains the spatiotemporal heterogeneity of fracture rates.

For geological formations in which faults already exist, fluid injection will change the porosity and permeability of the formation and subsequently reduce the formation strength, eventually leading to fault slippage. For the complete formation, the fluid-rock interaction in the formation will cause the softening and decomposition of mineral particles in the rock. The microstructure of the rock will gradually loosen, which can easily cause macroscopic mechanical damage to the rock. Experimental observations show that macro-fractures also occurred at a distance from the location of water injection (no obvious hydraulic connection channels). However, before the occurrence of the macro-fracture, the fluid had gathered at that location, indicating that small-scale hydraulic channels had existed, ensuring the possibility of water flow. Although pores are obviously good channels for fluid transport, certain areas, such as natural microfractures or weak zones of mineral cementation, are the most critical factor in the generation of fractures according to the experiment results.

Notably, the injected water may also change the surrounding stress field, which can easily cause the slip of a fault in the critical stress state. However, there is still a lack of intuitive experimental results to support this hypothesis.

4.4. Relevant limitations of this study

In this study, the fluid migration process within rocks can be observed from the perspective of the electromagnetic wave field based on in situ real-time CT scanning images. However, this method has limitations: analysing hydraulic fracture dynamic propagation solely through CT scanning images provides insufficient insight into the force interactions during rock failure, making it difficult to establish a bridge between fractures and stress. Although electromagnetic wave-based imaging can visualise rock matrix fracturing and fluid-solid coupling processes, it lacks the capability for the mechanical analysis of these processes. In particular, it cannot help elucidate the role of fluid seepage forces in hydraulic fracture propagation under different fracturing methods and cannot provide a comprehensive understanding of hydraulic fracture propagation laws in rocks. Passive acoustic emission real-time monitoring during experiments on rock hydraulic fracturing can effectively image the mechanical processes of the fracturing of a rock matrix under different fracturing methods from the perspective of a seismic wavefield.

In future studies, we aim to simultaneously conduct acoustic emission real-time monitoring and in situ real-time CT scanning during hydraulic fracturing experiments; moreover, we aim to jointly investigate the fracturing of a rock matrix under fluid-solid coupling and interactions between fluids and hydraulic fractures from the perspectives of both seismic and electromagnetic wavefields. This integrated approach will enable a more comprehensive understanding of the mechanisms of hydraulic fracture propagation.

5. Conclusions

In this study, for the first time, water-rock interactions and hydraulic fracture propagations inside sandstone samples during fluid injection experiments are completely presented by in situ dynamic X-ray CT. Based on this study, several conclusions can be summarised.

(1) Our experiments demonstrate that water-rock interactions can reduce rock strength, leading to macroscopic mechanical failure. Fluid flow pathways and changes in pore pressure are critical factors in the initiation of hydraulic fracture.
(2) Fractures preferentially nucleate at dry-wet interfaces associated with heterogeneous fluid distributions. Sustained high-pressure injection promotes shear fracture propagation along the maximum principal stress direction, forming complex fracture networks.
(3) The fracturing rate exhibits localised heterogeneity: rapid initial propagation decays owing to energy dissipation and roughening of the fracture surface.

In the future, we must conduct comparative studies on heterogeneous rocks (e.g. shale, carbonate) under stratigraphic conditions to refine fluid-driven fracture models. Moreover, we aim to combine acoustic emission and in situ dynamic X-ray CT to realise joint multiphysics monitoring, resolving spatiotemporal anisotropy in deep subsurface fracture networks.

CRediT authorship contribution statement

Zizhuo Ma: Writing – original draft, Methodology, Data curation. **Yibo Wang:** Writing – review & editing, Methodology, Conceptualization. **Liang Zhao:** Writing – review & editing. **Xinglin Lei:** Writing – review & editing. **Yikang Zheng:** Investigation. **Shaojiang Wu:** Investigation. **Qingfeng Xue:** Investigation.

Declaration of competing interest

The authors declare that they have no known competing financial interests or personal relationships that could have appeared to influence the work reported in this paper.

Acknowledgments

This work was supported by the National Science Fund for Distinguished Young Scholars (Grant No. 42025403) and the National Key R&D Program of China (Grant No. 2021YFA0716800).

Appendix A. Supplementary data

Supplementary data to this article can be found online at https://doi.org/10.1016/j.jrmge.2025.08.024.

References

Akbarabadi, M., Piri, M., 2013. Relative permeability hysteresis and capillary trapping characteristics of supercritical CO2/brine systems: an experimental study at reservoir conditions. Adv. Water Resour. 52, 190–206.

Alhosani, A., Scanziani, A., Lin, Q., Foroughi, S., Alhammadi, A.M., Blunt, M.J., Bijeljic, B., 2020. Dynamics of water injection in an oil-wet reservoir rock at subsurface conditions: invasion patterns and pore-filling events. Phys. Rev. E 102 (2), 023110.

Atkinson, G.M., Eaton, D.W., Ghofrani, H., Walker, D., Cheadle, B., Schultz, R., Shcherbakov, R., Tiampo, K., Gu, J., Harrington, R.M., 2016. Hydraulic fracturing and seismicity in the Western Canada sedimentary basin. Seismol Res. Lett. 87 (3), 631–647.

Atkinson, G.M., Eaton, D.W., Igonin, N., 2020. Developments in understanding seismicity triggered by hydraulic fracturing. Nat. Rev. Earth Environ. 1 (5), 264–277.

Arthur, J.D., Bohm, B., Layne, M., 2009. Hydraulic fracturing considerations for natural gas wells of the Marcellus Shale. Gulf Coast Assoc. Geol. Soc. Trans. 59, 49–59.

Bao, X., Eaton, D.W., 2016. Fault activation by hydraulic fracturing in Western Canada. Science 354 (6318), 1406–1409.

Benson, P.M., Austria, D.C., Gehne, S., Butcher, E., Harnett, C.E., Fazio, M., Rowley, P., Tomas, R., 2020. Laboratory simulations of fluid-induced seismicity, hydraulic fracture, and fluid flow. Geomech. Energy Environ. 24, 100169.

Berchenko, I., Detournay, E., 1997. Deviation of hydraulic fractures through poroelastic stress changes induced by fluid injection and pumping. Int. J. Rock Mech. Min. Sci. 34 (6), 1009–1019.

Bohloli, B., De Pater, C., 2006. Experimental study on hydraulic fracturing of soft rocks: influence of fluid rheology and confining stress. J. Pet. Sci. Eng. 53 (1–2), 1–12.

Bongole, K., Sun, Z., Yao, J., Mehmood, A., Yueying, W., Mboje, J., Xin, Y., 2019. Multifracture response to supercritical CO2-EGS and water-EGS based on thermo-hydro-mechanical coupling method. Int. J. Energy Res. 43 (13), 7173–7196.

Cao, W., Yildirim, B., Durucan, S., Wolf, K.-H., Cai, W., Agrawal, H., Korre, A., 2021. Fracture behaviour and seismic response of naturally fractured coal subjected to true triaxial stresses and hydraulic fracturing. Fuel 288, 119618.

Cartwright-Taylor, A., Main, I.G., Butler, I.B., Fusseis, F., Flynn, M., King, A., 2020. Catastrophic failure: how and when? Insights from 4-D in situ X-Ray microtomography. J. Geophys. Res. Solid Earth 125 (8), e2020JB019642.

Cesca, S., Grigoli, F., Heimann, S., González, A., Buforn, E., Maghsoudi, S., Blanch, E., Dahm, T., 2014. The 2013 September–October seismic sequence offshore Spain: a case of seismicity triggered by gas injection? Geophys. J. Int. 198 (2), 941–953.

Cui, Z.-D., Liu, D.-A., Zeng, R.-S., Niu, J.-R., Wang, H.-J., Shi, X.-S., 2013. Resistance of caprock to hydraulic fracturing due to CO2 injection into sand lens reservoirs. Eng. Geol. 164, 146–154.

Delle Piane, C., Clennell, M.B., Keller, J.V., Giwelli, A., Luzin, V., 2017. Carbonate hosted fault rocks: a review of structural and microstructural characteristic with implications for seismicity in the upper crust. J. Struct. Geol. 103, 17–36.

Du, K., Li, X., Tao, M., Wang, S., 2020. Experimental study on acoustic emission (AE) characteristics and crack classification during rock fracture in several basic lab tests. Int. J. Rock Mech. Min. Sci. 133, 104411.

Ellsworth, W.L., 2013. Injection-induced earthquakes. Science 341 (6142), 1225942.

Eyre, T.S., Eaton, D.W., Garagash, D.I., Zecevic, M., Venieri, M., Weir, R., Lawton, D.C., 2019. The role of aseismic slip in hydraulic fracturing–induced seismicity. Sci. Adv. 5 (8), eaav7172.

Foulger, G.R., Wilson, M.P., Gluyas, J.G., Julian, B.R., Davies, R.J., 2018. Global review of human-induced earthquakes. Earth Sci. Rev. 178, 438–514.

Frohlich, C., Hayward, C., Stump, B., Potter, E., 2011. The dallas–fort worth earthquake sequence: october 2008 through may 2009. Bull. Seismol. Soc. Am. 101 (1), 327–340.

Frohlich, C., Ellsworth, W., Brown, W.A., Brunt, M., Luetgert, J., MacDonald, T., Walter, S., 2014. The 17 may 2012 M4.8 earthquake near timpson, East Texas: an event possibly triggered by fluid injection. J. Geophys. Res. Solid Earth 119 (1), 581–593.

Gehne, S., Benson, P., Koor, N., Dobson, K., Enfield, M., Barber, A., 2019. Seismo-mechanical response of anisotropic rocks under hydraulic fracture conditions: new experimental insights. J. Geophys. Res. Solid Earth 124 (9), 9562–9579.

Grigoli, F., Cesca, S., Rinaldi, A.P., Manconi, A., Lopez-Comino, J.A., Clinton, J., Westaway, R., Cauzzi, C., Dahm, T., Wiemer, S., 2018. The November 2017 Mw 5.5 Pohang earthquake: a possible case of induced seismicity in South Korea. Science 360 (6392), 1003–1006.

Healy, J., Rubey, W., Griggs, D., Raleigh, C., 1968. The Denver earthquakes. Science 161 (3848), 1301–1310.

House, L., 1987. Locating microearthquakes induced by hydraulic fracturing in crystalline rock. Geophys. Res. Lett. 14 (9), 919–921.

Hu, Y., Wang, Z., 2018. Plate interactions, crustal deformation and magmatism along the eastern margins of the Tibetan Plateau. Tectonophysics 740, 10–26.

Ishida, T., Aoyagi, K., Niwa, T., Chen, Y., Murata, S., Chen, Q., Nakayama, Y., 2012. Acoustic emission monitoring of hydraulic fracturing laboratory experiment with supercritical and liquid CO2. Geophys. Res. Lett. 39 (16).

Jiang, L., Wu, B., Song, Y., Yang, M., Wang, D., Liu, Y., Xue, Z., 2017. Mass transfer coefficient measurement during brine flush in a CO2-filled packed bed by X-ray CT scanning. Int. J. Heat Mass Tran. 115, 615–624.

Kim, K.-H., Ree, J.-H., Kim, Y., Kim, S., Kang, S.Y., Seo, W., 2018. Assessing whether the 2017 Mw 5.4 Pohang earthquake in South Korea was an induced event. Science 360 (6392), 1007–1009.

Kwiatek, G., Martínez-Garzón, P., Plenkers, K., Leonhardt, M., Zang, A., Von Specht, S., Dresen, G., Bohnhoff, M., 2018. Insights into complex subdecimeter fracturing processes occurring during a water injection experiment at depth in Äspö Hard Rock laboratory, Sweden. J. Geophys. Res. Solid Earth 123 (8), 6616–6635.

Lajtai, E., 1974. Brittle fracture in compression. Int. J. Fract. 10, 525–536.

Lee, K.-K., Ellsworth, W.L., Giardini, D., Townend, J., Ge, S., Shimamoto, T., Yeo, I.-W., Kang, T.-S., Rhie, J., Sheen, D.-H., 2019. Managing injection-induced seismic risks. Science 364 (6442), 730–732.

Lei, X., Kusunose, K., Rao, M., Nishizawa, O., Satoh, T., 2000. Quasi-static fault growth and cracking in homogeneous brittle rock under triaxial compression using acoustic emission monitoring. J. Geophys. Res. Solid Earth 105 (B3), 6127–6139.

Lei, X., Funatsu, T., Ma, S., Liu, L., 2016. A laboratory acoustic emission experiment and numerical simulation of rock fracture driven by a high-pressure fluid source. J. Rock Mech. Geotech. Eng. 8 (1), 27–34.

Lei, X., Huang, D., Su, J., Jiang, G., Wang, X., Wang, H., Guo, X., Fu, H., 2017. Fault reactivation and earthquakes with magnitudes of up to Mw4.7 induced by shale-gas hydraulic fracturing in Sichuan Basin, China. Sci. Rep. 7 (1), 1–12.

Lei, X., Wang, Z., Su, J., 2019. The December 2018 ML 5.7 and January 2019 ML 5.3 earthquakes in South Sichuan basin induced by shale gas hydraulic fracturing. Seismol Res. Lett. 90 (3), 1099–1110.

Lei, X., Su, J., Wang, Z., 2020. Growing seismicity in the Sichuan Basin and its association with industrial activities. Sci. China Earth Sci. 63 (11), 1633–1660.

Li, L., Tan, J., Wood, D.A., Zhao, Z., Becker, D., Lyu, Q., Shu, B., Chen, H., 2019. A review of the current status of induced seismicity monitoring for hydraulic fracturing in unconventional tight oil and gas reservoirs. Fuel 242, 195–210.

Li, L., Blomberg, A.J., Spengler, J.D., Coull, B.A., Schwartz, J.D., Koutrakis, P., 2020. Unconventional oil and gas development and ambient particle radioactivity. Nat. Commun. 11 (1), 1–8.

Li, X., Lei, X., Shen, H., Li, Q., 2023. Fracturing around dry/wet boundary in tight sandstones monitored by micro-seismicity in laboratory. Rock Mech. Rock Eng. 56 (5), 3693–3708.

Liu, Y., Li, H., Luo, C., Wang, X., 2014. In situ stress measurements by hydraulic fracturing in the Western route of South to North Water Transfer project in China. Eng. Geol. 168, 114–119.

Liu, Q., Liang, B., Sun, W., Zhao, H., Hao, J., Hou, M., 2022. Experimental study on hydraulic fracturing of bedding shale considering anisotropy effects. ACS Omega 7 (26), 22698–22713.

Ma, Z., Wang, Y., Zheng, Y., 2022. In situ dynamic X-ray imaging of fluid-rock interactions inside tight sandstone during hydraulic fracturing: fluid flow process and fracture network growth. J. Pet. Sci. Eng. 214, 110490.

Majer, E.L., Baria, R., Stark, M., Oates, S., Bommer, J., Smith, B., Asanuma, H., 2007. Induced seismicity associated with enhanced geothermal systems. Geothermics 36 (3), 185–222.

Maxwell, S.C., Rutledge, J., Jones, R., Fehler, M., 2010. Petroleum reservoir characterization using downhole microseismic monitoring. Geophysics 75 (5), 75A129–75A137.

Naoi, M., Hirano, S., Chen, Y., 2025. High-resolution monitoring of hydraulically induced acoustic emission activities using neural phase picking and matched filter analysis. Prog. Earth Planet. Sci. 12 (1), 24.

Ning, W., Ju, W., Guo, W., 2024. The present-day in situ stress field and its effect on shale gas development in Zigong area of southern Sichuan Basin. Unconv. Resour. 4, 100078.

Patmonoaji, A., Zhang, Y., Xue, Z., Park, H., Suekane, T., 2019. Experimental and numerical simulation of supercritical CO2 microbubble injection into a brine-saturated porous medium. Int. J. Greenh. Gas Control 91, 102830.

Peña Castro, A., Roth, M., Verdecchia, A., Onwuemeka, J., Liu, Y., Harrington, R., Zhang, Y., Kao, H., 2020. Stress chatter via fluid flow and fault slip in a hydraulic fracturing-induced earthquake sequence in the Montney Formation, British Columbia. Geophys. Res. Lett. 47 (14), e2020GL087254.

Rabbel, O., Mair, K., Galland, O., Grühser, C., Meier, T., 2020. Numerical modeling of fracture network evolution in organic-rich shale with rapid internal fluid generation. J. Geophys. Res. Solid Earth 125 (7), e2020JB019445.

Renard, F., Cordonnier, B., Kobchenko, M., Kandula, N., Weiss, J., Zhu, W., 2017. Microscale characterization of rupture nucleation unravels precursors to faulting in rocks. Earth Planet Sci. Lett. 476, 69–78.

Renard, F., McBeck, J., Kandula, N., Cordonnier, B., Meakin, P., Ben-Zion, Y., 2019.

Volumetric and shear processes in crystalline rock approaching faulting. Proc. Natl. Acad. Sci. USA 116 (33), 16234–16239.
Rodriguez, I.V., Stanchits, S., 2017. Spatial and temporal variation of seismic attenuation during hydraulic fracturing of a sandstone block subjected to triaxial stress. J. Geophys. Res. Solid Earth 122 (11), 9012–9030.
Rubinstein, J.L., Ellsworth, W.L., McGarr, A., Benz, H.M., 2014. The 2001–present induced earthquake sequence in the raton basin of northern New Mexico and southern Colorado. Bull. Seismol. Soc. Am. 104 (5), 2162–2181.
Rutledge, J.T., Phillips, W.S., Mayerhofer, M., 2004. Faulting induced by forced fluid injection and fluid flow forced by faulting: an interpretation of hydraulic-fracture microseismicity, carthage cotton valley gas field, Texas. Bull. Seismol. Soc. Am 94 (5), 1817–1830.
Schoenball, M., Ajo-Franklin, J.B., Blankenship, D., Chai, C., Chakravarty, A., Dobson, P., Hopp, C., Kneafsey, T., Knox, H.A., Maceira, M., 2020. Creation of a mixed-mode fracture network at mesoscale through hydraulic fracturing and shear stimulation. J. Geophys. Res. Solid Earth 125 (12), e2020JB019807.
Schultz, R., Wang, R., 2020. Newly emerging cases of hydraulic fracturing induced seismicity in the Duvernay East Shale basin. Tectonophysics 779, 228393.
Schultz, R., Skoumal, R.J., Brudzinski, M.R., Eaton, D., Baptie, B., Ellsworth, W., 2020. Hydraulic fracturing-induced seismicity. Rev. Geophys. 58 (3), e2019RG000695.
Shapiro, S.A., Dinske, C., 2009. Fluid-induced seismicity: pressure diffusion and hydraulic fracturing. Geophys. Prospect. 57 (2), 301–310.
Shelly, D.R., Peng, Z., Hill, D.P., Aiken, C., 2011. Triggered creep as a possible mechanism for delayed dynamic triggering of tremor and earthquakes. Nat. Geosci. 4 (6), 384–388.
Shi, J.-Q., Xue, Z., Durucan, S., 2011. Supercritical CO2 core flooding and imbibition in Tako sandstone–influence of sub-core scale heterogeneity. Int. J. Greenh. Gas Control 5 (1), 75–87.
Song, J., Leng, J., Li, J., Wei, H., Li, S., Wang, F., 2025. Application of acoustic emission technique in landslide monitoring and early warning: a review. Appl. Sci. 15 (3), 1663.
Tan, Y., Hu, J., Zhang, H., Chen, Y., Qian, J., Wang, Q., Zha, H., Tang, P., Nie, Z., 2020. Hydraulic fracturing induced seismicity in the southern Sichuan Basin due to fluid diffusion inferred from seismic and injection data analysis. Geophys. Res. Lett. 47 (4), e2019GL084885.
Van Offenwert, S., Cnudde, V., Bultreys, T., 2019. Pore-scale visualization and quantification of transient solute transport using fast microcomputed tomography. Water Resour. Res. 55 (11), 9279–9291.
Vásárhelyi, B., 2006. Analysing the crack coalescence in brittle rock materials. Acta Geod. Geophys. Hung. 41, 181–198.
Velcin, H., Dautriat, J., Sarout, J., Esteban, L., Godel, B., 2020. Experimental reactivation of shear-fractured Berea and Boise sandstones by brine or liquid CO2 injection at depth. J. Geophys. Res. Solid Earth 125 (2), e2019JB018281.
Wang, Y., Li, X., Zhang, B., 2016. Numerical modeling of variable fluid injection-rate modes on fracturing network evolution in naturally fractured formations. Energies 9 (6), 414.
Wang, B., Chen, X., Chen, J., Yao, J., Tan, K., 2020. Elastic characteristics and petrophysical modeling of the Jurassic tight sandstone in Sichuan Basin. Chin. J. Geophys. 63 (12), 4528–4539.
Wang, Z., Wang, J., Yang, X., 2021. The role of fluids in the 2008 MS 8.0 Wenchuan earthquake. J. Geophys. Res. Solid Earth 126 (2), e2020JB019959.
Watanabe, N., Ishibashi, T., Ohsaki, Y., Tsuchiya, Y., Tamagawa, T., Hirano, N., Okabe, H., Tsuchiya, N., 2011. X-ray CT based numerical analysis of fracture flow for core samples under various confining pressures. Eng. Geol. 123 (4), 338–346.
Watanabe, N., Ishibashi, T., Tsuchiya, N., Ohsaki, Y., Tamagawa, T., Tsuchiya, Y., Okabe, H., Ito, H., 2013. Geologic core holder with a CFR PEEK body for the X-ray CT-based numerical analysis of fracture flow under confining pressure. Rock Mech. Rock Eng. 46 (2), 413–418.
Wei, C., Yu, L., Geng, S., Yuan, Z., Wang, Y., 2024. Experimental and numerical studies on propagation behavior between hydraulic fractures and pre-existing fractures under prepulse combined hydraulic fracturing. J. Rock Mech. Geotech. 17 (5), 2879–2892.
Wenning, Q.C., Madonna, C., Kurotori, T., Pini, R., 2019. Spatial mapping of fracture aperture changes with shear displacement using X-ray computerized tomography. J. Geophys. Res. Solid Earth 124 (7), 7320–7340.
Wilson, M., Worrall, F., Davies, R., Hart, A., 2017. Shallow aquifer vulnerability from subsurface fluid injection at a proposed shale gas hydraulic fracturing site. Water Resour. Res. 53 (11), 9922–9940.
Withers, P.J., Bouman, C., Carmignato, S., Cnudde, V., Grimaldi, D., Hagen, C.K., Maire, E., Manley, M., Du Plessis, A., Stock, S.R., 2021. X-ray computed tomography. Nat. Rev. Methods Primers 1 (1), 1–21.
Xia, Y., Yao, M., Li, T., Yang, H., Tang, C.A., 2024. Numerical analysis of hydraulic fracture propagation in deep shale reservoir with different injection strategies. J. Rock Mech. Geotech. Eng. 16 (9), 3558–3574.
Yang, H., Liu, Y., Lin, J., 2012. Effects of subducted seamounts on megathrust earthquake nucleation and rupture propagation. Geophys. Res. Lett. 39 (24).
Yang, H., Zhou, P., Fang, N., Zhu, G., Xu, W., Su, J., Meng, F., Chu, R., 2020. A shallow shock: the 25 February 2019 ML 4.9 earthquake in the Weiyuan shale gas field in Sichuan, China. Seismol Res. Lett. 91 (6), 3182–3194.
Yeo, I., Brown, M., Ge, S., Lee, K., 2020. Causal mechanism of injection-induced earthquakes through the Mw 5.5 Pohang earthquake case study. Nat. Commun. 11 (1), 1–12.
Zang, A., Stephansson, O., Stenberg, L., Plenkers, K., Specht, S., Milkereit, C., Schill, E., Kwiatek, G., Dresen, G., Zimmermann, G., 2017. Hydraulic fracture monitoring in hard rock at 410 m depth with an advanced fluid-injection protocol and extensive sensor array. Geophys. J. Int. 208 (2), 790–813.
Zang, A., Zimmermann, G., Hofmann, H., Niemz, P., Kim, K.Y., Diaz, M., Zhuang, L., Yoon, J.S., 2021. Relaxation damage control via fatigue-hydraulic fracturing in granitic rock as inferred from laboratory-, mine-, and field-scale experiments. Sci. Rep. 11 (1), 1–16.
Zhang, H., Eaton, D.W., Rodriguez, G., Jia, S.Q., 2019. Source-mechanism analysis and stress inversion for hydraulic-fracturing-induced event sequences near fox creek, Alberta. Bull. Seismol. Soc. Am. 109 (2), 636–651.
Zhang, B., Hu, Y., Hu, X., Xu, Q., 2023. Fluid-solid coupling mechanism of shale hydraulic fracture propagation based on true triaxial test and numerical analysis. Lithosphere 2022 (Special 12), 5085244.

Zizhuo Ma received her BSc degree in exploration technology and engineering from Jilin University and her PhD degree in solid geophysics from the Institute of Geology and Geophysics, Chinese Academy of Sciences. She is currently working at the Geophysical Technology Research Institute of Sinopec Petroleum Exploration and Production Research Institute. Her research interests include multiphysics monitoring and analysis of hydraulic fracture propagation processes, rock elastic properties measurement and modeling.